



Decisive role of hybridized electronic states on the appearance of superconductivity in $\text{Ba}_{1-x}\text{K}_x\text{MO}_3$ ($M = \text{Bi}, \text{Sb}$)

Julien Varignon ^{*}*Laboratoire CRISMAT, CNRS UMR 6508, ENSICAEN, Normandie Université, 6 boulevard Maréchal Juin, F-14050 Caen Cedex 4, France* (Received 15 May 2023; revised 9 July 2024; accepted 26 August 2024; published 10 September 2024)

The observation of superconductivity (SC) in hole-doped antimonates $\text{Ba}_{1-x}\text{K}_x\text{SbO}_3$ (BKSO), isoelectronic compounds to bismuthate $\text{Ba}_{1-x}\text{K}_x\text{BiO}_3$ (BKBO) SCs, enables a pathway to clarify the role of hybridizations between electronic states of metals and ligands on the emergence of SC. Herein, using first-principles simulations, the localized electronic structure of antimonates is demonstrated to produce various charge and bond orderings (CBOs) up to $x = 0.6$, hence hindering the appearance of a SC state. This is in contrast with bismuthates where the formation of charge orderings is suppressed by doping effects and their native hybridized electronic structure. Although quenched by doping effects, the CBOs mediate the Cooper pair formation, and the resulting electron-phonon coupling reproduces the experimental facts such as a larger T_c in BKSO than in BKBO for $x > 0.65$ and a maximal T_c of ~ 30 K observed at $x = 0.4 - 0.5$ for BKBO. The latter point is ascribed to a soft phonon mode at $x = 0.5$, while the former observation is ascribed to an intrinsically stronger coupling between lattice distortions and electrons in BaSbO_3 . Although materials with a localized electronic structure could warrant larger T_c s, the main drawback is the resilience of such compounds to form a metallic state, and hence SC emerges far away of soft phonons possessing a strong coupling with the electronic structure.

DOI: [10.1103/PhysRevB.110.125120](https://doi.org/10.1103/PhysRevB.110.125120)

I. INTRODUCTION

Superconductivity (SC) is certainly one of the most fascinating property of materials characterized by zero electrical resistance to direct current and perfect diamagnetism. It is explained based on bound electrons forming Cooper pairs [1]. In the Bardeen-Cooper-Schrieffer (BCS) theory [2], the formation of Cooper pairs is explained by exchange of phonons. In many other systems, proximity of a charge-ordered (CO) state or a magnetic phase transition is proposed to be a key behind the formation of bound electrons. Strong correlation effects that must be considered in electronic structure simulations [3–11] and/or strong hybridizations between metals and anionic p states [12–15] are also proposed to be a determining factor behind SC.

One can usually quantify the level of hybridization between the metal and the anionic O states by evaluating the charge transfer energy ΔE_{CT} , that is, the energy difference between the center of the bands associated with relevant metallic (E_m) and oxygen (E_o) levels (i.e., $\Delta E_{CT} = E_m - E_o$). A negative (positive) ΔE_{CT} then corresponds to strongly (weakly) hybridized and hence delocalized (localized) electronic structures. These two types of regimes are therefore coined as negative and positive charge transfer (NCT and PCT) regimes, respectively. Emblematic examples of materials falling within the NCT regime are the cuprates or the bismuthates that are both SCs once appropriately doped with electrons and/or holes [3, 12, 16–18]. However, the lack of isoelectronic SCs long hindered the exploration of the precise role of

hybridizations between metals and anion states on the emergence of SC in oxides. The discovery of SC in hole-doped BaSbO_3 (BSO), an isoelectronic material to bismuthates $\text{Ba}_{1-x}\text{K}_x\text{BiO}_3$ but that belongs to the PCT regime, thus offers an ideal testbed for clarifying the role of hybridizations [19].

In bulk, BSO adopts a slightly distorted ABO_3 perovskite structure characterized by a bond disproportionation B_{oc} mode producing a rock-salt pattern of compressed O_6 groups and extended octahedra [Fig. 1(a)]. It originates from an unstable 4+ formal oxidation state (FOS) of Sb cations ($5s^1$ electronic configuration) that prefers to disproportionate to the more stable 3+ ($5s^2$) and 5+ ($5s^0$) FOSs in the ground state [20], yielding a CO insulating state with Sb cations sitting in extended (Sb^{3+}) and compressed (Sb^{5+}) octahedra. Once sufficiently doped with holes by forming a $\text{Ba}_{1-x}\text{K}_x\text{SbO}_3$ solid solution ($0.65 < x < 0.8$), the material becomes a SC with a critical temperature T_c up to 15 K for $x = 0.65$ [19].

At first glance, the observation of SC in hole-doped BSO is expected since it is isostructural and isoelectronic to bismuthates (BaBiO_3 and SrBiO_3) that both exhibit SC once appropriately hole doped [16, 18, 21, 22]. Nevertheless, these two families of compounds show noticeable differences: (i) the doping content needed to transit from a charge- and bond-ordered (CBO) insulating state to the SC region is smaller in $\text{Ba}_{1-x}\text{K}_x\text{BiO}_3$ (BKBO, $x \sim 0.4$) than in $\text{Ba}_{1-x}\text{K}_x\text{SbO}_3$ (BKSO, $x > 0.6$); (ii) BSO falls within the PCT regime with $\Delta E_{CT} = 0.76$ eV, while BaBiO_3 is in a NCT regime with $\Delta E_{CT} = -2.45$ eV [19]; (iii) T_c reaches 32 K in BKBO around $x = 0.4 - 0.5$ [18, 21], while it does not exceed 15 K in the optimally doped BKSO [19]; and (iv) BKSO exhibits larger T_c s than BKBO for $x > 0.65$. Although a triggered mechanism between octahedral rotations and the

^{*}Contact author: julien.varignon@ensicaen.fr

disproportionation effects could promote a strong stability of the B_{oc} mode [23,24], this possibility is ruled out by an apparent absence of octahedral rotations in antimonates. One may thus ask: (i) Possessing the same roots in the undoped starting phase, is SC also reached at the proximity of a CBO state in BKSO as in BKBO (and $Sr_{1-x}K_xBiO_3$)? (ii) What is the intrinsic difference responsible for the largest doping content needed to reach the SC region in BKSO than in BKBO? (iii) What are the determining factors behind the larger T_c exhibited by BKSO than BKBO for $x > 0.65$? (iv) Why is the maximal T_c of BKBO larger than that of optimally doped BKSO?

In this paper, using density functional theory (DFT) involving all relevant degrees of freedom and a parameter-free meta-generalized gradient approximation (GGA)-revised strongly constrained and appropriately normalized (R2SCAN) [25] functional, antimonates are identified to possess a stronger electronic instability toward charge- and bond-disproportionation effects associated with the unstable 4+ FOS of B -site cations than bismuthates. This strong tendency to form CBO is resilient to hole doping BKSO for $x = 0$ to 0.6, thereby hindering the apparition of a metallic phase. This is ascribed to the ionic nature of the electronic structure of antimonates that favors a localized state. In contrast, the NCT nature and the resulting delocalized electronic structure of bismuthates already screen the tendency toward disproportionation, thereby requiring a lower doping content to transit to a metallic phase. Once doping totally quenches the formation of the various CBOs, the electron-phonon couplings (EPCs) associated with the CBO remain sufficiently large to mediate the formation of Cooper pairs. Nevertheless, the EPCs for $x > 0.65$ are larger in BKSO than in BKBO due to a stronger coupling between structural displacements and the electronic structure, resulting in larger T'_c 's for BKSO than for BKBO at a fixed doping content. Finally, the maximal T_c reached at $x = 0.5$ in BKBO originates from a CBO phonon mode that reaches a low frequency at $x = 0.5$, thereby producing a maximal EPC. Thus, although materials with a localized electronic structure possess a strong coupling between structural distortions and electrons, the drawback of such compounds is their resilience to doping effects, thereby hindering the emergence of a SC phase close to soft phonon modes.

II. METHODS

A. DFT simulations

DFT calculations are performed with VASP [26,27]. To appropriately amend the self-interaction errors inherent to practiced DFT, the R2SCAN [25] functional is employed. This type of meta-GGA functional was previously shown to be accurate in capturing the correct trend of insulating to SC transition as a function of doping content in isoelectronic and isostructural bismuthates [24]. It further allows a parameter-free calculation with a functional that can adapt to different FOSs showed by a single ion. The energy cutoff is set to 650 eV, and atomic positions plus lattice parameters are optimized until forces acting on each atom are < 0.005 eV/Å. Projector augmented-wave [28] potentials are used for modeling core electrons with the following VASP

5.4 Perdew-Burke-Ernzerhof POTCAR files: Ba_sv, K_sv, Sb, Bi, and O. The cation substitutions are extracted by using the special quasirandom structure, allowing us to identify the cation arrangement maximizing the disorder characteristic of a solid solution [29]. This was successfully applied to capture trends in insulator-to-metal transition through doping effects in $Sr_{1-x}K_xBiO_3$ [24] or in $Sm_{1-x}Ca_xNiO_3$ solid solutions [30]. The atomic positions are provided in Tables SI1 and SI2 in Supplemental Material 1 [31]. Solid solutions are modeled by using 32 f.u. corresponding to a $(2\sqrt{2}, 2\sqrt{2}, 4)$ supercell, or 27 f.u. with a $(3,3,3)$ supercell, with respect to the high-symmetry primitive $Pm - 3m$ cell exhibited by perovskite materials. Several structural starting points are considered for each doping content, corresponding to potential lattice distortions that can localize electrons. For instance, a CO $Ba_{2/3}K_{1/3}SbO_3$ should correspond to a material with 1 Sb^{3+} and 2 $Sb^{5+/s}$; it should then induce a distortion with a \vec{q} vector of either $(\frac{1}{3}, 0, 0)$, $(\frac{1}{3}, \frac{1}{3}, 0)$, or $(\frac{1}{3}, \frac{1}{3}, \frac{1}{3})$. To reduce the computational effort, preliminary checks are performed on smaller unit cells compatible with a given distortion mode and doping content. Then these cells are transformed into larger supercells to have a better representation of the solid solution with 32 or 27 f.u.

B. SC quantities

Using the methodology presented in Ref. [32], the EPC constant λ is computed as

$$\lambda = \frac{2N(E_F)}{N_{\vec{q}}} \sum_{\vec{q}, \nu} \frac{\hbar^2}{2M_X \omega_{\vec{q}, \nu}^2} |D_{\vec{q}}^{\nu}|^2, \quad (1)$$

where $N(E_F)$ is the density of states (DOS) at the Fermi level E_F , $N_{\vec{q}}$ is the number of \vec{q} points considered, M_X is the mass of moving atoms, $\omega_{\vec{q}, \nu}$ is the frequency of mode ν at point \vec{q} , and $|D_{\vec{q}}^{\nu}|$ is the reduced electron-phonon matrix element (REPME). The latter quantity is extracted by estimating the band splitting ΔE_b induced by the addition of the eigendisplacement of the (\vec{q}, ν) phonon mode in the ground state with the amplitude $u_{\vec{q}, \nu}$ per moving atom:

$$D_{\vec{q}}^{\nu} = \left| \frac{\Delta E_b}{2u_{\vec{q}, \nu}} \right|. \quad (2)$$

The frequency $\omega_{\vec{q}, \nu}$ of mode ν at point \vec{q} is obtained by fitting the total energy E vs mode amplitude $Q_{\vec{q}, \nu}$ of a (\vec{q}, ν) phonon starting from the ground-state structure with a polynomial expression of the form $E(Q_{\vec{q}, \nu}) = aQ_{\vec{q}, \nu}^2 + bQ_{\vec{q}, \nu}^4$. Recalling that the energy of a harmonic oscillator is given by $\frac{1}{2}M_X \omega_{\vec{q}, \nu}^2 Q_{\vec{q}, \nu}^2$, the frequency $\omega_{\vec{q}, \nu}$ is

$$\omega_{\vec{q}, \nu} = \sqrt{\frac{2a}{M_X}}. \quad (3)$$

The critical temperature T_c of the material is computed using the Mc Millan-Allen equation [33]:

$$T_c = \frac{\hbar \omega_{\log}}{1.2} \exp \left[-\frac{1.04\lambda}{\lambda - \mu^*(1 + 0.62\lambda)} \right], \quad (4)$$

where μ^* is the screened Coulomb potential with typical values between 0.1 and 0.15, and ω_{\log} is the logarithmic

frequency estimated as

$$\omega_{\log} = \left(\prod_i^n \omega_i \right)^{1/n}. \quad (5)$$

C. Wannier functions

To extract localized atomiclike functions, Wannier functions (WFs) are built from the DFT band structure. To that end, the 10 Kohn-Sham states located around the Fermi level for a primitive cubic cell are projected on initial guess functions of B s (1 state) and O p (9 states) characters to get the initial gauge for the localization procedure [34–36]. The DOS can then be built based on these localized atomiclike functions. Using the on-site energies associated with the WFs, the charge transfer energy is computed as the energy difference $\Delta E_{CT} = E_s - E_p$.

D. Other details

Band structures are unfolded to the primitive high-symmetry $Pm\bar{3}m$ cell of perovskites using the VASPBANDUNFOLD code [37]. Symmetry of relaxed structures are obtained using FINDSYM [38], and amplitudes of distortions with respect to a primitive high-symmetry $Pm\bar{3}m$ cell are extracted using AMPLIMODES of the Bilbao Crystallographic Server [39] and the ISOTROPY suite of software [40].

III. RESULTS AND DISCUSSION

A. Electronic structure of bulk BaSbO₃

Electronic and structural properties of pristine BaSbO₃ are first studied. After the structural relaxation of the bulk material, BaSbO₃ is identified to adopt a $R\bar{3}$ structure at 0 K characterized by an $a^-a^-a^-$ antiphase octahedral rotation in Glazer's notation as well as a bond disproportionation B_{oc} mode. From a symmetry mode analysis with respect to the primitive high-symmetry $Pm\bar{3}m$ cell adopted by perovskites, the octahedral rotation (labeled \emptyset) and B_{oc} distortion exhibit sizeable amplitude of distortions with $Q_{\emptyset} = 0.130 \text{ \AA}/\text{f.u.}$ and $Q_{B_{oc}} = 0.191 \text{ \AA}/\text{f.u.}$, respectively. The amplitude of B_{oc} is in sharp agreement with the experimental value of $Q_{B_{oc}} = 0.187 \text{ \AA}/\text{f.u.}$ extracted from the structure at 300 K from Ref. [19]. It is worth emphasizing that no octahedral rotations have been identified at 300 K, but they likely appear at lower temperature. The energy-lowering event associated with the O₆ rotations with respect to a cell with only the B_{oc} mode is indeed extremely small ($\Delta E = -0.7 \text{ meV}/\text{f.u.}$). This is also suggested by an imaginary frequency of the \emptyset mode from the first-principles calculations on BaSbO₃ presented in Ref. [41].

The effect of the B_{oc} mode is to split the Sb cations into two different cations [Fig. 1(a)]: a Sb cation sits in an extended octahedra (labeled Sb_L), while all its first nearest-neighbor Sb cations are located in a compressed O₆ group (labeled Sb_S). It hence produces a clear asymmetry of the electronic structure between the two types of Sb cations and opens a band gap of 0.90 eV, as shown by the projected DOS reported in Fig. 1(b). One further notices that Sb_L cations are fully occupied, in contrast with Sb_S cations that show partly unoccupied s states,

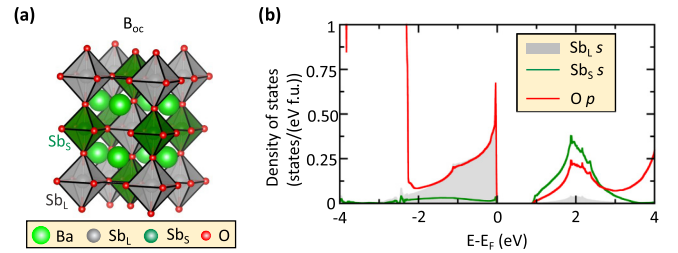


FIG. 1. Structural and electronic properties of BaSbO₃. (a) Breathing (B_{oc}) structural distortion exhibited by BaSbO₃ and producing different O₆ groups around Sb cations. (b) Projected density of states on Sb_L (filled gray area) and Sb_S (green line) s states and O p states (red line) around the Fermi level in the $R\bar{3}$ ground state.

compatible with disproportionation effects. Finally, one observes that unoccupied states are predominantly formed by the B cation states rather than O p states, hinting at the fact that this compound is characterized by a localized electronic structure rather than by Bi s and O p hybridized states as in BaBiO₃, see Supplemental Material 2 [31].

B. Doped phase diagram

Figure 2 displays the phase diagram of BKSO solid solutions as a function of x . At low doping content $x = 0.125$, two bipolaronic states are stabilized in the material with holes created on Sb_L cations that are doubly occupied in the pristine material. This is accompanied by the collapsing of the local O₆ octahedra due to the increase of the FOS of the local Sb cations. The average B_{oc} mode amplitude decreases to $Q_{B_{oc}} = 0.161 \text{ \AA}/\text{f.u.}$ for $x = 0.125$, albeit it is sufficient to produce a semiconducting state with a band gap of 0.74 eV. Further increasing the doping content transforms the system into a metal at $x = 0.25$, yet with a persistent breathing mode B_{oc} . The latter only vanishes at $x = 0.4375$.

Although one would expect a metallic non-CBO phase above $x = 0.25$, alternative bond disproportionation distortions, labeled alt- $B_{oc1/3}$ and alt- $B_{oc1/2}$ and sketched in Fig. 2, emerge for $x = \frac{1}{3}$ and 0.50. These lattice distortions are associated with peculiar CO producing large octahedra and compressed O₆ groups accommodating a given charge ordering. These modes reach their maxima at $x = 0.5$ and $\frac{1}{3}$, which correspond to Ba_{0.5}K_{0.5}SbO₃ and Ba_{0.66}K_{0.33}SbO₃ solutions, respectively. At $x = 0.5(\frac{1}{3})$, Sb cations are in a nominally 4.5+ (4.33+) FOS, but in fact they prefer to disproportionate into $4\text{Sb}^{4.5+} \rightarrow 3\text{Sb}^{5+} + \text{Sb}^{3+}$ ($3\text{Sb}^{4.33+} \rightarrow 2\text{Sb}^{5+} + \text{Sb}^{3+}$) in the ground state. Above $x = 0.5$, all solutions are found metallic without the presence of B_{oc} and alt- B_{oc} modes. Hence, all types of CO vanish for $x > 0.5625$.

The existence of multiple CBOs is compatible with experiments showing two distinct CBOs in the doped phase diagram of antimonates up to $x > 0.5625$ [20]. Notably, a distortion pattern compatible with one large O₆ group (Sb³⁺) surrounded by three smaller octahedra (Sb⁵⁺) at $x = 0.5$ has been reported experimentally, although the symmetry is different from the DFT result- I_4/mmm space group with the present DFT vs I_4/mcm in Ref. [20]. This slight discrepancy may originate from the limited supercell size used in the simulations. The existence of a bond disproportionation appearing at the M

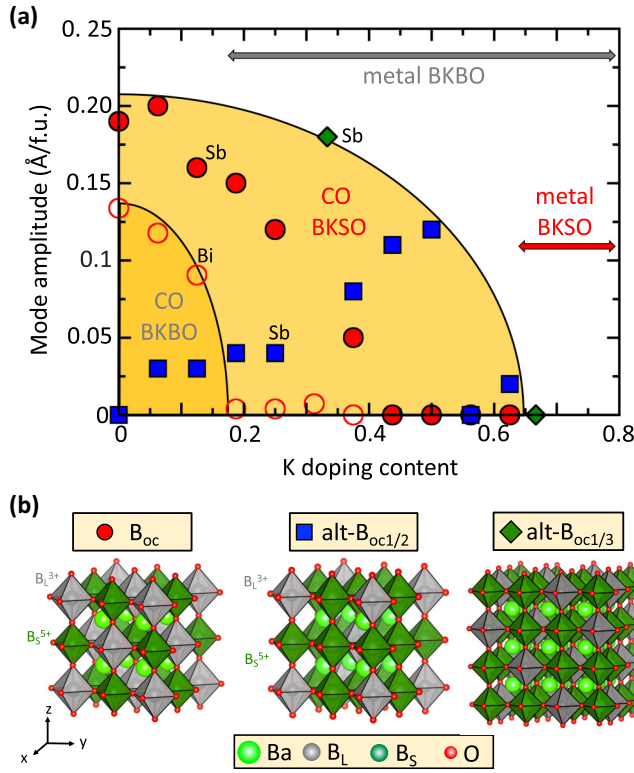


FIG. 2. Doped phase diagram of antimonates and bismuthates. (a) Evolution of the B_{oc} (red circles), $alt-B_{oc1/2}$ (blue squares), and $alt-B_{oc1/3}$ (green diamonds) mode amplitude (in $\text{\AA}/f.u.$) as a function of the doping content x in $Ba_{1-x}K_xSbO_3$ (filled symbols) compound and $Ba_{1-x}K_xBiO_3$ (unfilled symbols). (b) Sketches of the three main bond disproportionation modes identified in doped antimonates. B_{oc} , $alt-B_{oc1/2}$, and $alt-B_{oc1/3}$ appear at the $(\frac{1}{2}, \frac{1}{2}, \frac{1}{2})$, $(\frac{1}{2}, \frac{1}{2}, 0)$, and $(\frac{1}{3}, \frac{1}{3}, 0)$ points of the Brillouin zone.

point $[\vec{q} = (\frac{1}{2}, \frac{1}{2}, 0)]$ is also suggested by DFT calculations of Ref. [41] with the existence of an imaginary frequency in the cubic cell of $x = 0.5$ doped antimonates. Furthermore, the extinction of all CBOs closely relates with the appearance of the SC region experimentally ($x > 0.6$). It is worth emphasizing that the R2SCAN functional may slightly underestimate the band gaps and hence might shift the insulating-to-metal-to-SC transition as a function of x to slightly smaller doping contents than the experimentally observed content. The existence of multiple CBOs in BKSO is surprising since isoelectronic BKBO does not develop such a propensity toward the $alt-B_{oc}$ modes, for instance. Indeed, similar structural relaxations in BKBO only reveal a B_{oc} mode that is rapidly quenched upon doping (Fig. 2). One concludes here that the SC transition of antimonates (and bismuthates) is at the vicinity of a stable CO phase.

C. Potential energy surfaces associated with disproportionation modes

To understand the different response to hole-doping effects between BKBO and BKSO, potential energy surfaces (PESs)

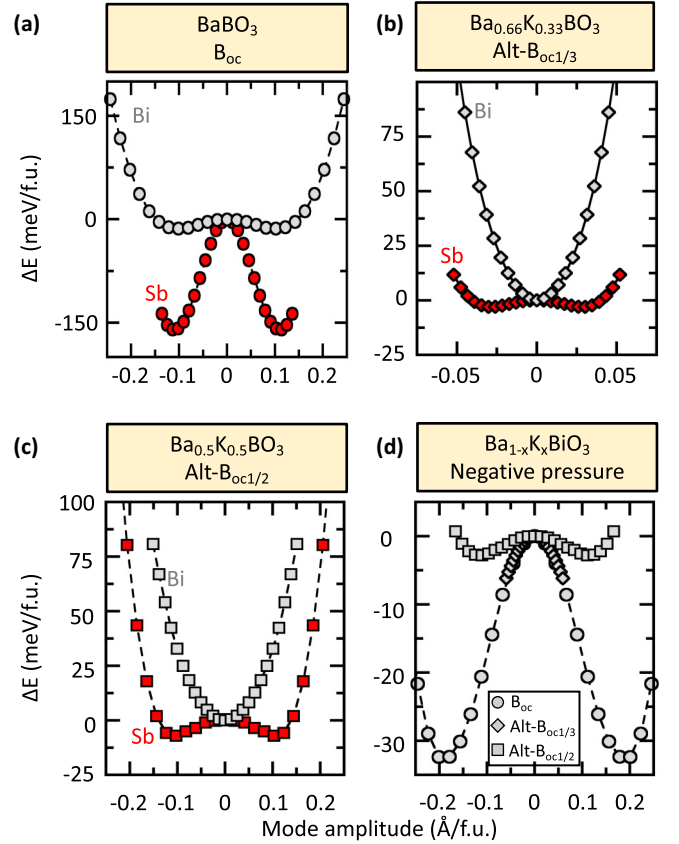


FIG. 3. Potential energy surfaces associated with the B_{oc} and $alt-B_{oc}$ structural distortions. Energy gain ΔE (in $\text{meV}/f.u.$) associated with the condensation of amplitudes (in $\text{\AA}/f.u.$) of either B_{oc} (circles), $alt-B_{oc1/3}$ (diamonds), or $alt-B_{oc1/2}$ (squares) in 0, 33, and 50% doped $BaSbO_3$ (in red) and $BaBiO_3$ (in gray) starting from a high-symmetry cubic cell with a lattice parameter yielding the ground-state volume of relaxed doped compounds. (d) A negative pressure expanding the cubic cell parameter by 10% is also considered. The reference energy is taken at zero amplitude of the modes. Irreducible representation are R_2^- , M_1^+ , and LD_1 for B_{oc} , $alt-B_{oc1/2}$, and $alt-B_{oc1/3}$ distortions, respectively, when the A site cation is considered at the corner of the cell.

associated with disproportionation distortions starting from a perfectly undistorted high-symmetry $Pm-3m$ cell are computed at $x = 0, 0.33$, and 0.50 [Figs. 3(a)–3(c)]. At $x = 0$, the B_{oc} mode PES is characterized by a double-well potential whose minimum is located at nonzero amplitude for the two materials. It follows that the B_{oc} mode spontaneously appears in the compounds, signaling the presence of an instability toward disproportionation effects of the $4+$ FOS of Sb and Bi cations. Nevertheless, the B_{oc} mode is associated with a large energy gain in $BaSbO_3$ ($\Delta E = -160 \text{ meV}/f.u.$), while it is much smaller in $BaBiO_3$ ($\Delta E = -15 \text{ meV}/f.u.$). Regarding the $alt-B_{oc1/2}$ and $alt-B_{oc1/3}$ modes at $x = 0.5$ and 0.33 , respectively, double-well potentials with a minimum located at nonzero amplitude are identified in $BaSbO_3$, while $BaBiO_3$ does not have a propensity to develop these alternative disproportionation modes.

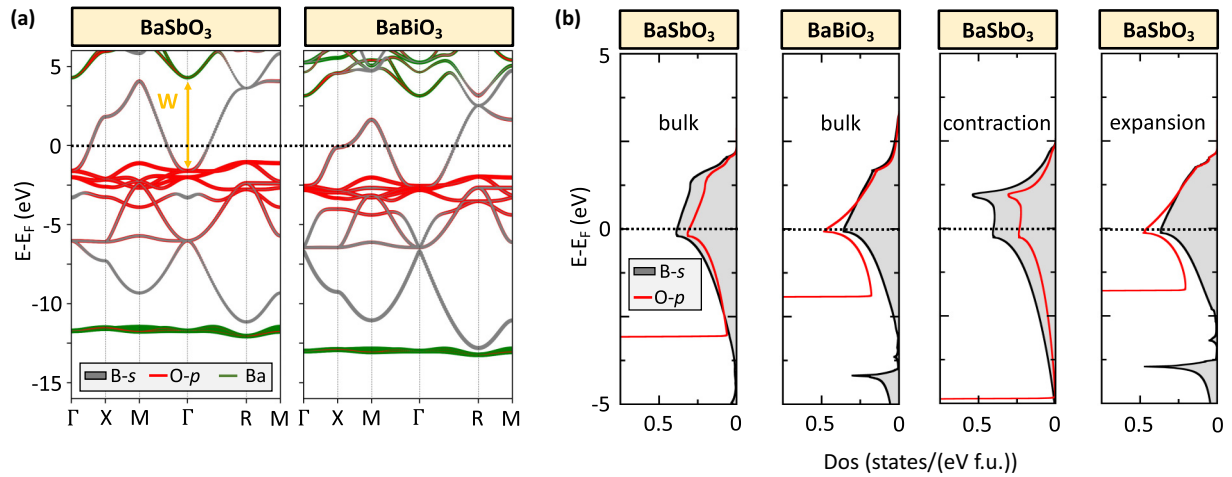


FIG. 4. Electronic properties of cubic cells. (a) Band structure within the cubic cell of BaSbO₃ and BaBiO₃ projected on B s (gray), O p states (red), and Ba (green) contributions. (b) Projected density of states (DOS) on B s (gray) and O p states (red) in BaSbO₃ and BaBiO₃ in bulk and in BaSbO₃ with a cell expansion/contraction of 5% of the cubic lattice parameter. The horizontal dashed line corresponds to the Fermi level. The high-symmetry points are Γ (0,0,0), X ($\frac{1}{2}, 0, 0$), M ($\frac{1}{2}, \frac{1}{2}, 0$), and R ($\frac{1}{2}, \frac{1}{2}, \frac{1}{2}$). The DOS is plotted based on Wannier functions.

D. Localized (hybridized) electronic structures are at the core of the multiple (absence of) CBOs

The tendency to develop instabilities toward disproportionation effects or Jahn-Teller effects is strongly dependent on the level of hybridization between relevant B cation and O p states as well as the compacity of bands in perovskites [42–45], i.e., compact states increase correlation effects, while hybridizations screen them. To understand the different tendency in disproportionation effects between BKSO and BKBO, one can start from a cubic cell of the pristine compounds. By looking at the projected band structure on B s and O p states of Fig. 4(a), one identifies that (i) the bandwidth W 's of states undergoing disproportionation effects are more compact in BBO ($W = 5.12$ eV) than in BSO ($W = 5.78$ eV), and (ii) the band crossing the Fermi level is dominantly of B s character in BSO, while it is dominantly of O p character in BBO. Point (ii) is further confirmed by projected DOS on B s and O p characters presented in Fig. 4(b). By adjusting the lattice parameter of each compound by $\pm 5\%$, the bandwidth W as well as the hybridized character of states are driven by geometric effects [Figs. 4(b) and 5(a)]: W decreases with increasing the cell volume, while the B cation character of bands crossing the Fermi level increases with decreasing the cell volume.

The role of W and hybridizations on the tendency toward disproportionation effects can be tracked by recomputing the PESs of the B_{oc} mode for the two compounds but with lattice parameters expanded or contracted by 5%. The energy gain ΔE associated with the stabilization of the B_{oc} mode as well as the fractional amplitude Q_{Boc} of stabilized B_{oc} mode are reported in Fig. 5 (PESs are available in Supplemental Material 3 [31]). In both cases, the tendency toward disproportionation effect increases with increasing the cell volume, but energy gains are an order of magnitude larger in BSO than in BBO. The very same trend is observed for the stabilized amplitude Q_{Boc} of the B_{oc} mode in the structure. The increased tendency toward disproportionation effect with increasing the lattice parameter is explained by a reduced bandwidth in both compounds. Even though BBO and BSO would exhibit the

same lattice parameter, ΔE in BBO would remain an order of magnitude smaller than in BSO. This is because the O p character of the states crossing the Fermi level ultimately increases and becomes dominant over B cation states [Fig. 4(b)] with increasing the cell volume, thereby screening the tendency toward disproportionation effects. Therefore, the larger tendency toward disproportionation effect of BSO with respect to BBO is explained by the intrinsically more ionic character of its electronic structure and hence its more correlated nature.

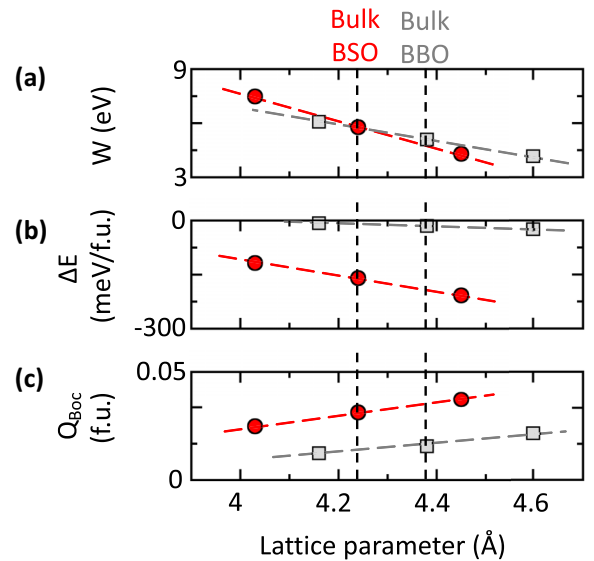


FIG. 5. Trends of disproportionation effects as a function of the cubic cell lattice parameter. (a) Evolution of the bandwidth W (in eV), (b) energy gain associated with the condensation of the B_{oc} mode (in meV/f.u.), and (c) fractional amplitude Q_{Boc} of stabilized B_{oc} mode (in fractional units) starting from a perfectly undistorted cell of compounds as a function of the lattice parameter in BaSbO₃ (in red) and BaBiO₃ (in gray). The normalized Q_{Boc} is obtained by dividing the amplitude of distortions by the cell parameter.

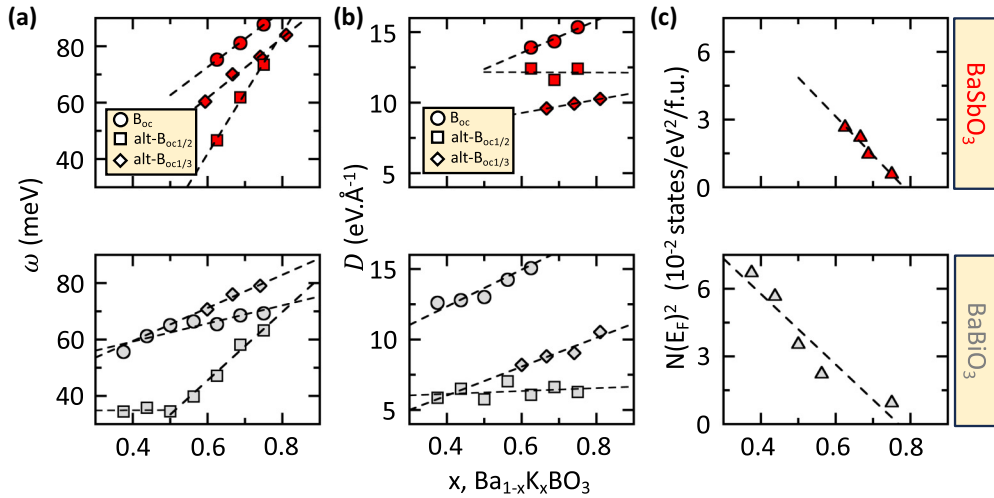


FIG. 6. Superconducting quantities. (a) Frequency ω (in meV), (b) reduced electron phonon matrix element D (in $\text{eV}/\text{\AA}$) for the B_{oc} (circles), $\text{alt-}B_{oc1/2}$ (squares), and $\text{alt-}B_{oc1/3}$ (diamonds) modes, and (c) squared density of states at the Fermi level $N(E_F)^2$ (in $\text{states}/\text{eV}^2/\text{f.u.}$) in BaSbO_3 (red) and BaBiO_3 (gray). The dashed lines correspond to linear fits of the density functional theory (DFT) results.

The hybridized electronic structure of BaBiO_3 then explains the fact that the $\text{alt-}B_{oc1/2}$ and $\text{alt-}B_{oc1/3}$ are not stabilized in $\text{Ba}_{1-x}\text{K}_x\text{BiO}_3$ for $x = \frac{1}{2}$ and $\frac{1}{3}$, respectively. To confirm this result, the bandwidth W of relevant states undergoing the disproportionation effects is decreased to $W = 3.88$ eV by applying a cell parameter expansion of 10% vs $W = 6.20$ eV for the bulk phase. It then produces a slight double-well potential for the $\text{alt-}B_{oc1/2}$ mode, albeit its energy gain ($\Delta E_{\text{alt-}B_{oc1/2}} = -2.8$ meV/f.u.) remains smaller than that observed in unpressured antimonates ($\Delta E_{\text{alt-}B_{oc1/2}} = -7.1$ meV/f.u.). The observation of quenched disproportionation modes with hybridization and doping effects is in sharp agreement with experiments: BKSO becomes a SC for $x > 0.65$, while BKBO is SC for $x > 0.35$. One concludes here that doping as well as hybridized electronic structures are a knob quenching all CBOs.

E. SC properties

Being able to produce an insulating state in the underdoped regime of BKSO and BKBO and be quenched by doping and hybridization effects, one may wonder if CBO lattice vibrations can produce a sufficiently large EPC for explaining Cooper pair formation and the SC temperature in the appropriately doped region. Figure 6 reports the main SC quantities of doped BaSbO_3 and BaBiO_3 necessary to compute the EPC with Eq. (1) (band structures of doped compounds are presented in Supplemental Material 4 [31]). In BaSbO_3 , the frequency of the different disproportionation modes increases with increasing the doping content in the SC region. Such a behavior is also observed in BaBiO_3 at the exception of the $\text{alt-}B_{oc1/2}$ mode that only increases for $x > 0.5$ and is nearly constant with a minimum at $x = 0.5$. This is explained by the fact that this mode is compatible with a half-doped situation that would result in a charge ordering with $4\text{Bi}^{4.5+}$ transforming to $3\text{Bi}^{5+} + 1\text{Bi}^{3+}$, should the material be characterized by a localized electronic structure.

The REPMEs, labeled D , increase with increasing the doping content for all disproportionation modes, with the

exception of the $\text{alt-}B_{oc1/2}$ mode that shows a constant value with x . One highlights that the REPMEs are globally larger in BaSbO_3 than in BaBiO_3 , with the exception of the B_{oc} mode that has roughly the same magnitude in both compounds. This closely relates to the appearance of this mode in the pristine form of both materials. The larger REPMEs for $\text{alt-}B_{oc}$ modes in BaSbO_3 likely originate from the PCT nature and hence more localized electronic structure of antimonates inducing a stronger electron-electron interaction.

Regarding the squared DOS for several doped compounds, one observes a linear trend as a function of the doping content x . This is compatible with a free electron gas in which the DOS evolves as $\sqrt{(E - E_0)}$; the doping content x is acting on the $E - E_0$ value, where E_0 is the bottom of the parabola. Finally, it is worth emphasizing that the squared DOS is larger in BKBO than in BKSO, compatible with the fact that the bandwidth is smaller in BaBiO_3 than in BaSbO_3 .

Figure 7(a) displays the evolution of the EPC associated with each CBO in BKSO and BKBO as a function of the doping content and obtained from fits of $N(E_F)$, D , and ω as a function of the doping content (see Supplemental Material 5 [31]). All EPCs decrease with increasing the doping content, in agreement with the extinction of the tendency toward CBO identified at lower doping content. The optimally doped BKBO ($x = 0.4 - 0.5$) presents a total EPC, computed as the average of the EPC induced by the three disproportionation modes [see Eq. (1)] ~ 1 , in agreement with experimental values suggesting an EPC of 1.3 ± 0.2 [8] and previous theoretical works [9–11,24]. This EPC then rapidly decreases and becomes smaller than the total EPC of BKSO for $x > 0.6$. This agrees with previous DFT calculations showing such a trend [10]. Finally, the $\text{alt-}B_{oc1/2}$ and $\text{alt-}B_{oc1/3}$ modes have a larger contribution to the total EPC in BKSO than in BKBO for $x > 0.65$, thereby producing a larger total EPC in BKSO for these doping contents.

One can then estimate the critical temperature T_c using the modified MacMillan equation presented in Eq. (4), where ω_{\log} is the logarithmic averaged phonon frequency (expressed in K), and μ^* is the screened Coulomb potential with

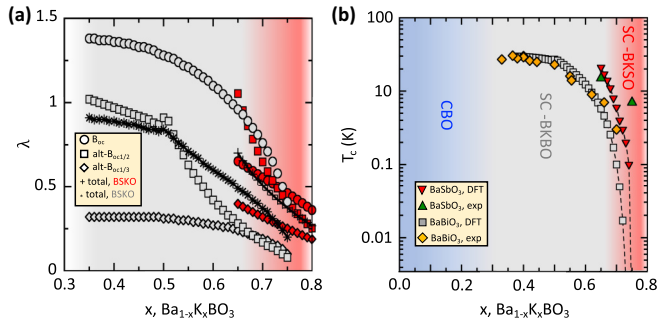


FIG. 7. Superconducting properties of $\text{Ba}_{1-x}\text{K}_x\text{SbO}_3$ and $\text{Ba}_{1-x}\text{K}_x\text{BiO}_3$ compounds. Computed electron-phonon coupling constant (a) λ associated with the B_{oc} (circles), $\text{alt-B}_{\text{oc}1/2}$ (squares), and $\text{alt-B}_{\text{oc}1/3}$ (diamonds) modes in BKSO (red) and BKBO (gray) and (b) computed critical temperature T_c (in K) vs the doping content in BaSbO_3 (down red triangles) and BaBiO_3 (gray squares). A screened Coulomb potential $\mu^* = 0.125$ is used. Experimental values for BaBiO_3 (orange diamonds) and BaSbO_3 (up green triangles) are extracted from Refs. [19,46,47].

conventional values usually ranging from 0.1 to 0.15. Considering the three disproportionation modes as the characteristic frequencies and assimilating $\omega_{\text{log}} = (\omega_{\text{Boc}}\omega_{\text{alt-Boc}1/2}\omega_{\text{alt-Boc}1/3})^{1/3}$ and a usual screened Coulomb potential $\mu^* = 0.125$, a T_c of 22 K is obtained in $\text{Ba}_{0.35}\text{K}_{0.65}\text{SbO}_3$, and a maximal T_c of 30 K is extracted in BKBO for $x = 0.4 - 0.5$ [Fig. 7(b)]. These results are in good agreement with experimental values available in the literature with a maximal T_c of 15 K in BKSO ($x = 0.65$) and 32 K in optimally doped BKBO. Furthermore, the global trend of T_c vs doping content is well captured by the model, highlighting that the identified disproportionation modes are the determining factor behind the SC mechanism of antimonates and bismuthates. It is worth emphasizing that (i) the DFT model may underestimate the doping content needed to reach the SC phase due to band gap underestimation inherent to semilocal DFT functionals, and (ii) there are, of course, uncertainties on T_c associated with the choice of μ^* and the approximation for estimating ω_{log} .

Ionic nature of antimonates explains large T_c for $x > 0.65$. At the same doping content, such as $x = 0.65$, the T_c of antimonates is predicted to be higher (22 K) than the T_c of bismuthates (5.7 K), compatible with experimental facts (15 vs 7 K in BKSO and BKBO, respectively, Ref. [19]). Although the B_{oc} mode yields very similar EPC λ for the two

compounds, the alternative disproportionation modes $\text{alt-B}_{\text{oc}1/2}$ and $\text{alt-B}_{\text{oc}1/3}$ have a larger contribution to the total EPC in antimonates than in bismuthates, resulting in a larger EPC in BKSO [Fig. 7(a)]. The larger EPCs originate from a stronger coupling between these structural motions and the electronic structure [$D_{\text{Boc}1/2} = 12.5 \text{ eV \AA}^{-1}$ in BKSO and 6 eV \AA^{-1} in BKBO, Fig. 6(b)].

alt-B_{oc}1/2 mode explains maximal T_c centered at $x = 0.5$ in BKBO. Due to its NCT nature, the alt-B_{oc} disproportionation modes are already quenched by the hybridized electronic structure in BKBO. Nevertheless, the $\text{alt-B}_{\text{oc}1/2}$ mode remains compatible with a half-doped situation, and it hence reaches its lowest frequency at $x = 0.4 - 0.5$. For $x > 0.5$, the mode rapidly hardens upon doping the compound [Fig. 6(a)]. Recalling that λ is inversely proportional to ω^2 [Eq. (1)], the EPC associated with $\text{alt-B}_{\text{oc}1/2}$ is maximal for $x = 0.4 - 0.5$. It results in a plateau for T_c between $x = 0.4$ and 0.5 [Fig. 7(b)], in agreement with experiments.

IV. CONCLUSIONS

The ionic character and resulting more localized electronic structure of $\text{Ba}_{1-x}\text{K}_x\text{SbO}_3$ explains the high doping content needed to reach the SC phase in the doping phase diagram. At the same time, it produces strongly coupled structural-electronic features sufficient to mediate the formation of Cooper pairs. Nevertheless, the drawback is the resilience of the material to transit to a metallic state with doping and hence to the emergence of a SC state close to soft phonons strongly coupled to the electrons. This situation is reminiscent of the SC nickelates, where the starting material is a strong Mott insulator prone to exhibit several CBOs upon doping before transiting the SC region for high doping content [32]. Finally, identifying the relevant and potentially hidden electronic and structural instabilities in the doped phase diagram of compounds is a critical aspect for understanding the emergence of SC.

ACKNOWLEDGMENTS

J.V. acknowledges access granted to HPC resources of Criann through Projects No. 2020005 and No. 2007013 and of Cines through the DARI Project No. A0080911453. This paper was supported by the French ANR through the project ‘‘SuperNickel.’’

- [1] L. N. Cooper, Bound electron pairs in a degenerate Fermi gas, *Phys. Rev.* **104**, 1189 (1956).
- [2] J. Bardeen, L. N. Cooper, and J. R. Schrieffer, Theory of superconductivity, *Phys. Rev.* **108**, 1175 (1957).
- [3] B. Keimer, S. A. Kivelson, M. R. Norman, S. Uchida, and J. Zaanen, From quantum matter to high-temperature superconductivity in copper oxides, *Nature (London)* **518**, 179 (2015).

- [4] A. Garg, M. Randeria, and N. Trivedi, Strong correlations make high-temperature superconductors robust against disorder, *Nat. Phys.* **4**, 762 (2008).
- [5] H. Li, X. Zhou, S. Parham, T. J. Reber, H. Berger, G. B. Arnold, and D. S. Dessau, Coherent organization of electronic correlations as a mechanism to enhance and stabilize high- T_c cuprate superconductivity, *Nat. Commun.* **9**, 26 (2018).

- [6] P. Worm, L. Si, M. Kitatani, R. Arita, J. M. Tomczak, and K. Held, Correlations tune the electronic structure of pentalayer nickelates into the superconducting regime, *Phys. Rev. Mater.* **6**, L091801 (2022).
- [7] M. Kitatani, L. Si, O. Janson, R. Arita, Z. Zhong, and K. Held, Nickelate superconductors—A renaissance of the one-band Hubbard model, *npj Quantum Mater.* **5**, 59 (2020).
- [8] C. H. P. Wen, H. C. Xu, Q. Yao, R. Peng, X. H. Niu, Q. Y. Chen, Z. T. Liu, D. W. Shen, Q. Song, X. Lou *et al.*, Unveiling the superconducting mechanism of $\text{Ba}_{0.51}\text{K}_{0.49}\text{BiO}_3$, *Phys. Rev. Lett.* **121**, 117002 (2018).
- [9] Z. P. Yin, A. Kutepov, and G. Kotliar, Correlation-enhanced electron-phonon coupling: Applications of *GW* and screened hybrid functional to bismuthates, chloronitrides, and other high- T_c superconductors, *Phys. Rev. X* **3**, 021011 (2013).
- [10] Z. Yuan, P. Zheng, Y. Peng, R. Liu, X. Ma, G. Wang, T. Yu, and Z. Yin, Correlation-enhanced electron-phonon coupling and superconductivity in $(\text{Ba}, \text{K})\text{SbO}_3$ superconductors, *Phys. Rev. B* **105**, 014517 (2022).
- [11] Z. Li, G. Antonius, M. Wu, F. H. Da Jornada, and S. G. Louie, Electron-phonon coupling from *ab initio* linear-response theory within the *GW* method: Correlation-enhanced interactions and superconductivity in $\text{Ba}_{1-x}\text{K}_x\text{BiO}_3$, *Phys. Rev. Lett.* **122**, 186402 (2019).
- [12] F. C. Zhang and T. M. Rice, Effective Hamiltonian for the superconducting Cu oxides, *Phys. Rev. B* **37**, 3759 (1988).
- [13] L. F. Mattheiss and D. R. Haman, Electronic structure of $\text{BaPb}_{1-x}\text{Bi}_x\text{O}_3$, *Phys. Rev. B* **28**, 4227 (1983).
- [14] A. Khazraie, K. Foyevtsova, I. Elfimov, and G. A. Sawatzky, Bond versus charge disproportionation in the bismuth perovskites, *Phys. Rev. B* **98**, 205104 (2018).
- [15] M. R. Benam, K. Foyevtsova, A. Khazraie, I. Elfimov, and G. A. Sawatzky, Bond versus charge disproportionation and nature of the holes in $s - p \text{ABX}_3$ perovskites, *Phys. Rev. B* **104**, 195141 (2021).
- [16] S. M. Kazakov, C. Chaillout, P. Bordet, J. J. Capponi, M. Nunez-Regueiro, A. Rysak, J. L. Tholence, P. G. Radaelli, S. N. Putilin, and E. V. Antipov, Discovery of a second family of bismuth-oxide-based superconductors, *Nature (London)* **390**, 148 (1997).
- [17] J. G. Bednorz and K. A. Müller, Possible high T_c superconductivity in the Ba-La-Cu-O system, *Z. Phys. B* **64**, 189 (1986).
- [18] A. W. Sleight, Bismuthates: BaBiO_3 and related superconducting phases, *Physica C* **514**, 152 (2015).
- [19] M. Kim, G. M. McNally, H.-H. Kim, M. Oudah, A. S. Gibbs, P. Manuel, R. J. Green, R. Sutarto, T. Takayama, A. Yaresko *et al.*, Superconductivity in $(\text{Ba}, \text{K})\text{SbO}_3$, *Nat. Mater.* **21**, 627 (2022).
- [20] M. Kim, S. Klenner, G. M. McNally, J. Nuss, A. Yaresko, U. Wedig, R. K. Kremer, R. Pöttgen, and H. Takagi, Mixed valence and superconductivity in perovskite antimonates, *Chem. Mater.* **33**, 6787 (2021).
- [21] L. F. Mattheiss, E. M. Gyorgy, and D. W. Johnson, Superconductivity above 20 K in the Ba-K-Bi-O system, *Phys. Rev. B* **37**, 3745 (1988).
- [22] A. W. Sleight, J. L. Gillson, and P. E. Bierstedt, High-temperature superconductivity in the $\text{BaPb}_{1-x}\text{Bi}_x\text{O}_3$ system, *Solid State Commun.* **17**, 27 (1975).
- [23] A. Mercy, J. Bieder, J. Íñiguez, and P. Ghosez, Structurally triggered metal-insulator transition in rare-earth nickelates, *Nat. Commun.* **8**, 1677 (2017).
- [24] J. Varignon, Origin of superconductivity in hole doped SrBiO_3 bismuth oxide perovskite from parameter-free first-principles simulations, *npj Comput. Mater.* **9**, 30 (2023).
- [25] J. W. Furness, A. D. Kaplan, J. Ning, J. P. Perdew, and J. Sun, Accurate and numerically efficient R2SCAN meta-generalized gradient approximation, *J. Phys. Chem. Lett.* **11**, 8208 (2020).
- [26] G. Kresse and J. Furthmüller, Efficiency of *ab-initio* total energy calculations for metals and semiconductors using a plane-wave basis set, *Comput. Mater. Sci.* **6**, 15 (1996).
- [27] G. Kresse and J. Hafner, *Ab initio* molecular dynamics for liquid metals, *Phys. Rev. B* **47**, 558(R) (1993).
- [28] P. E. Blöchl, Projector augmented-wave method, *Phys. Rev. B* **50**, 17953 (1994).
- [29] A. Zunger, S.-H. Wei, L. G. Ferreira, and J. E. Bernard, Special quasirandom structures, *Phys. Rev. Lett.* **65**, 353 (1990).
- [30] L. Iglesias, M. Bibes, and J. Varignon, First-principles study of electron and hole doping effects in perovskite nickelates, *Phys. Rev. B* **104**, 035123 (2021).
- [31] See Supplemental Material at <http://link.aps.org/supplemental/10.1103/PhysRevB.110.125120> for containing the supercells used in the calculations as well as band structures of doped compound.
- [32] A. A. Carrasco-Alvarez, S. Petit, L. Iglesias, M. Bibes, W. Prellier, and J. Varignon, Electron-phonon mediated superconductivity in $\text{La}_6\text{Ni}_5\text{O}_{12}$ nickel oxides, [arXiv:2311.13674](https://arxiv.org/abs/2311.13674).
- [33] P. B. Allen and R. C. Dynes, Transition temperature of strongly-coupled superconductors reanalyzed, *Phys. Rev. B* **12**, 905 (1975).
- [34] G. Pizzi, V. Vitale, R. Arita, S. Blügel, F. Freimuth, G. Géranton, M. Gibertini, D. Gresch, C. Johnson, T. Koretsune *et al.*, WANNIER90 as a community code: New features and applications, *J. Phys.: Condens. Matter* **32**, 165902 (2020).
- [35] A. A. Mostofi, J. R. Yates, Y.-S. Lee, I. Souza, D. Vanderbilt, and N. Marzari, WANNIER90: A tool for obtaining maximally-localised Wannier functions, *Comput. Phys. Commun.* **178**, 685 (2008).
- [36] A. A. Mostofi, J. R. Yates, G. Pizzi, Y. S. Lee, I. Souza, D. Vanderbilt, and N. Marzari, An updated version of WANNIER90: A tool for obtaining maximally-localised Wannier functions, *Comput. Phys. Commun.* **185**, 2309 (2014).
- [37] V. Popescu and A. Zunger, Extracting E versus \vec{k} effective band structure from supercell calculations on alloys and impurities, *Phys. Rev. B* **85**, 085201 (2012).
- [38] H. T. Stokes and D. M. Hatch, FINDSYM: Program for identifying the space-group symmetry of a crystal, *J. Appl. Cryst.* **38**, 237 (2005).
- [39] D. Orobengoa, C. Capillas, M. I. Aroyo, and J. M. Perez-Mato, AMPLIMODES: Symmetry-mode analysis on the Bilbao Crystallographic Server, *J. Appl. Cryst.* **42**, 820 (2009).
- [40] ISOTROPY Software Suite, Iso.Byu.Edu, https://iso.byu.edu/iso/isodistort_version5.6.1/isodistort.php.
- [41] B. G. Jang, M. Kim, S.-H. Lee, W. Yang, S.-H. Jhi, and Y.-W. Son, Intersite Coulomb interactions in charge-ordered systems, *Phys. Rev. Lett.* **130**, 136401 (2023).
- [42] J. Varignon, M. Bibes, and A. Zunger, Origins versus fingerprints of the Jahn-Teller effect in d -electron ABX_3 perovskites, *Phys. Rev. Res.* **1**, 033131 (2019).

- [43] J. Varignon, M. Bibes, and A. Zunger, Origin of band gaps in $3d$ perovskite oxides, *Nat. Commun.* **10**, 1658 (2019).
- [44] J. Varignon, O. I. Malyi, and A. Zunger, Dependence of band gaps in d -electron perovskite oxides on magnetism, *Phys. Rev. B* **105**, 165111 (2022).
- [45] G. A. Baraff, E. O. Kane, and M. Schlüter, Theory of the silicon vacancy: An Anderson negative- U system, *Phys. Rev. B* **21**, 5662 (1980).
- [46] Y. Nagata, A. Mishiro, T. Uchida, M. Ohtsuka, and H. Samata, Normal-state transport properties of $\text{Ba}_{1-x}\text{K}_x\text{BiO}_3$ crystals, *J. Phys. Chem. Solids* **60**, 1933 (1999).
- [47] D. C. Kim, A. N. Baranov, J. S. Kim, H. R. Kang, B. J. Kim, Y. C. Kim, J. S. Pshirkov, E. V. Antipov, and Y. W. Park, Superconductivity of $\text{Ba}_{1-x}\text{K}_x\text{BiO}_3$ ($0.35 < x < 1$) synthesized by the high pressure and high temperature technique, *J. Supercond.* **15**, 331 (2002).